the target range for DRAM applications ($1–5 \times 10^{-7}$ A cm^{-2}). At this composition, we find $\epsilon_r = 62.5$ and the FOM is 24.3 μC cm^{-2}.

These results should be contrasted with those of bulk crystalline $Zr_xSn_yTi_zO_4$ ($x + y + z = 2$) (ref. 12). A single homogeneous solid-solution phase, isomorphous with the orthorhombic α-PbO_2 structure, was found near the composition $ZrTiO_4$, as indicated in Fig. 2. The remainder of the $Zr_xSn_yTi_zO_4$ phase diagram consists of multiphase mixtures of the ternary phase and the endmembers. Zr–Sn–Ti–O polycrystalline ceramics are well known for their superior microwave properties, including a moderate dielectric constant, very low dissipation factor, and low temperature coefficient of permittivity[13]. The properties of $Zr_{0.875}Sn_{0.25}Ti_{0.875}O_2$, for example, were studied carefully as a function of doping and sintering. A permittivity of ~36 and values for the dissipation factor (tan $\delta \sim 1/Q$) as low as 7×10^{-5} were obtained. The indicated composition is typical of those used for applications, which are invariably chosen to be within the homogeneous phase field. Note that the optimum compositions in our amorphous films are outside this composition field that yields homogeneous crystalline phases.

Amorphous thin films of (Zr, Sn)TiO_4 with a particular but unspecified Zr:Sn composition have been studied[14]: a value of $\epsilon_r = 27$ was inferred in amorphous films prepared by radio frequency magnetron sputtering at 200 °C; a value of $\epsilon_r = 38$ was found in crystalline films, that is, the bulk value. For approximately the same composition, however, we observe $\epsilon \sim 50$. This is a very substantial difference. At present we cannot explain the discrepancy between our data and those described in ref. 14. We do observe a decrease in the dielectric constant for deposition at higher temperatures, namely for films with a presumably greater degree of local order, so perhaps the films deposited by Nakagawara *et al.*[14] also have a higher degree of order than our films.

This work demonstrates the value of the CCS technique in the search for metastable materials whose properties are sensitive to preparation conditions. Many issues regarding the development of this material for practical application remain to be addressed. For example, fully optimized uniform films need to be made using a single target with on-axis sputtering (or using CVD), and the properties of films ~10–20 nm thick (one fifth the present value) must be evaluated. Also, conditions that lead to a lower leakage current must be found and capacitors made using standard electrodes (for example, TiN) must be subjected to standard post-processing and evaluated for reliability using accelerated testing. Although Zr–Sn–Ti–O films must be further developed, our preliminary results are encouraging. □

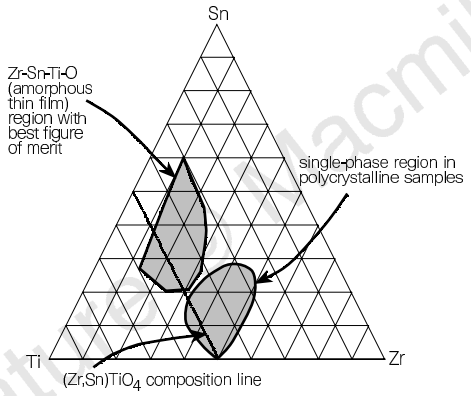

Figure 2 Representation of the ternary phase diagram of Zr–Ti–Sn–O. Shown is the region where single-phase crystalline material is obtained (horizontal hatching) compared to the region where the best thin-film properties are obtained (diagonal hatching), as inferred from Fig. 1b. The dark line indicates the (Zr, Sn)TiO_4 line composition, which reflects prior art shown in ref. 14.

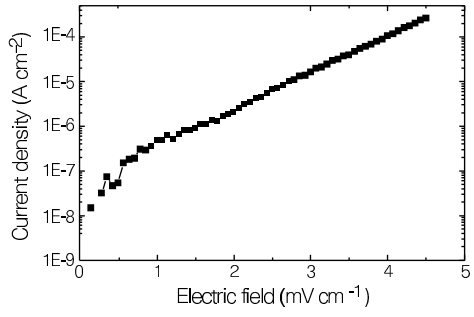

Figure 3 A typical current–voltage characteristic for a film with the approximate composition $Zr_{0.3}Ti_{0.9}Sn_{0.8}O_2$. The dielectric constant in this film was $\epsilon_r = 62.5$ (using the thickness determined by Rutherford backscattering, RBS, as 70 nm). The FOM for this film was 24.3 μC cm^{-2}.

Received 22 August; accepted 22 December 1997.

1. *The National Technology Roadmap for Semiconductors* page 123 (Sematech, Austin, 1994); also http://www.sematech.org/public/roadmap/ntrs94.pdf.
2. El-Kareh, B., Bronner, G. B. & Schuster, S. E. The evolution of DRAM cell technology. *Solid State Technol.* 89–101 (May 1997).
3. Gerstenberg, D. in *Handbook of Thin Film Technology* (eds Maissel, L. & Glang, R.) Ch. 19, page 8 (McGraw-Hill, New York, 1970).
4. Waser, R., Baiatu, T. & Härdtl, K.-H. DC electrical degradation of perovskite-type titanates: I, ceramics. *J. Am. Ceram. Soc.* **73,** 1645–1653 (1990).
5. Baiatu, T., Waser, R. & Härdtl, K.-H. DC electrical degradation of perovskite-type titanates: I, Ceramics. *J. Am. Ceram. Soc.* **73,** 1663–1673 (1990).
6. Kahawara, T., Yamamuka, M., Yuuki, A. & Ono, K. (Ba, Sr)TiO_3 films prepared by liquid source chemical vapor deposition on Ru electrodes. *Jpn. J. Appl. Phys.* **35,** 4880–4885 (1996).
7. Park, S. O. *et al.* Fabrication and electrical characterization of Pt/(Ba, Sr)TiO_3/Pt capacitors for ultralarge-scale integrated dynamic random access memory applications. *Jpn. J. Appl. Phys.* **35,** 1548–1552 (1996).
8. Basceri, C., Streiffer, S. K., Kingon, A. I. & Waser, R. The dielectric response as a function of temperature and film thickness of fiber-textured (Ba, Sr)TiO_3 thin films grown by chemical vapor deposition. *J. Appl. Phys.* **82,** 2497–2504 (1997).
9. Xiang, X.-D. *et al. Science* **268,** 1738–1740 (1995).
10. Sawatzky, E. & Kay, E. Cation deficiencies in RF sputtered gadolinium iron garnet films. *IBM J. Res. Dev.* **13,** 696–702 (1969).
11. Hanak, J. J. The 'multi-sample concept' in materials research: synthesis, compositional analysis and testing of entire multicomponent systems. *J. Mater. Sci.* **5,** 964–971 (1970).
12. Wolfram, G. & Göbel, H. Existence range, structural and dielectric properties of $Zr_xTi_ySn_zO_4$ ceramics ($x + y + z = 2$). *Mater. Res. Bull.* **16,** 1455–1463 (1981).
13. Iddles, D. M., Bell, A. J. & Moulson, A. J. Relationships between dopants, microstructure and the microwave dielectric properties of ZrO_2-TiO_2-SnO_2 ceramics. *J. Mater. Sci.* **27,** 6303–6310 (1992).
14. Nakagawara, O. *et al.* Electrical properties of (Zr, Sn)TiO_4 dielectric thin film prepared by pulsed laser deposition. *J. Appl. Phys.* **80,** 388–392 (1996).

Acknowledgements. We thank H. Huggins for TiN-coated Si substrates; Y.-H. Wong and D. W. Murphy for technical discussions; and R. A. Laudise for enthusiastic support of this project.

Correspondence and requests for materials should be addressed to R.B.v.D.

Decompression-induced melting of ice IV and the liquid–liquid transition in water

Osamu Mishima* & H. Eugene Stanley†

* *National Institute for Research in Inorganic Materials (NIRIM), 1-1, Namiki, Tsukuba, Ibaraki 305-0044, Japan*

† *Center for Polymer Studies and Department of Physics, Boston University, Boston, Massachusetts 02215, USA*

Although liquid water has been the focus of intensive research for over 100 years, a coherent physical picture that unifies all of the known anomalies of this liquid[1–3] is still lacking. Some of these anomalies occur in the supercooled region, and have been rationalized on the grounds of a possible retracing of the liquid–gas spinodal (metastability limit) line into the supercooled liquid region[4–7] or alternatively the presence of a line of first-order liquid–liquid phase transitions in this region which ends in a critical point[8–14]. But these ideas remain untested experimentally,

in part because supercooled water can be probed only above the homogeneous nucleation temperature T_H at which water spontaneously crystallizes. Here we report an experimental approach that is not restricted by the barrier imposed by T_H, involving measurement of the decompression-induced melting curves of several high-pressure phases of ice in small emulsified droplets. We find that the melting curve for ice IV seems to undergo a discontinuity at precisely the location proposed for the line of liquid–liquid phase transitions[8]. This is consistent with, but does not prove, the coexistence of two different phases of (supercooled) liquid water. From the experimental data we calculate a possible Gibbs potential surface and a corresponding equation of state for water, from the forms of which we estimate the coordinates of the liquid–liquid critical point to be at pressure $P_c \approx 0.1$ GPa and temperature $T_c \approx 220$ K.

In the liquid–liquid hypothesis for the anomalies of supercooled water[8], the liquid can exist in two phases of different densities, here denoted the high-density liquid (HDL) and low-density liquid (LDL) by analogy with the known high-density amorphous (HDA) and low-density amorphous (LDA) phases of ice[15]. To explore the region of the phase diagram in which this transition is supposed to occur, we have studied water confined to droplets with diameters of the order of 1–10 μm and exposed to high pressures (Fig. 1a). In such small volumes, nucleation of secondary ice phases following melting in the supercooled regime is kinetically suppressed. This procedure is especially useful in detecting metastable melting curves (Fig. 1b, c) and, as it is not affected by the presence of the line of homogeneous nucleation temperatures $T_H(P)$ (ref. 16) (below which melting is immediately followed by freezing), can be applied to provide a partial test for the hypothesis that there exists a line L_1 of liquid–liquid first-order phase transitions somewhere in the region of the P–T plane below the line $T_H(P)$. Any metastable melting line that crosses L_1 should display discontinuous behaviour at L_1 (such as ice IV shown in Fig. 1d) because the melting behaviour of the ice would be different for the two liquids that coexist at L_1.

We confine 1 cm^3 of water emulsion in an indium capsule and we compress (and decompress) it at a constant rate by a piston cylinder apparatus (Fig. 1a). We measure T using a thermocouple throughout the compression and decompression cycle. As an endothermic (or exothermic) transition results in a change in temperature (Fig. 1b), we can determine with high accuracy the location of the CIM (compression-induced melting) and DIM (decompression-induced melting) lines[16]. The present experiments reveal that discontinuous behaviour does occur on melting (Fig. 2). In the region of overlap, the DIM lines agree with the previously reported melting lines[17,18], confirming that they are indeed the equilibrium stable melting line and the equilibrium metastable melting line. Moreover, they disappear when we compress an emulsion-carrier sample without water. We confirm the production of the supercooled liquid on further decompression by finding an exothermic transition at the T_H line below 0.2 GPa, which indicates freezing of the liquid[19]. Crystalline ice appears, probably due to immediate freezing after melting occurs (below T_H, the transition to another crystalline phase should occur on the DIM line because the liquid produced by DIM should crystallize homogeneously below this temperature).

We extend the T_H line to 1.5 GPa by compressing the supercooled liquid and detecting its freezing on the T_H (Fig. 2a, centre panel). We also observe the CIM line for ice I_h, consistent with previous results[16] (note that we replace the nominal pressure reported in ref. 16 by the real pressure). We find the crystallization line, T_X, of emulsified HDA is higher by ~20 K than that of bulk HDA around 1.5 GPa; only the results are shown in Fig. 2a, right panel. The long-dashed line and the horizontal 'error bar' around 0.2 GPa in Fig. 2a, right panel, indicate the proposed[20] and the experimentally obtained[21] location of the LDA/HDA 'equilibrium' boundary. The long-dashed line around 0.5 GPa indicates the extrapolated I_h/HDA 'equilibrium' boundary.

We also find what appear to be two 'possible new phases' (PNP), denoted PNP-XIII and PNP-XIV. The DIM line for PNP-XIV is useful because it serves as a 'control' for the discontinuous

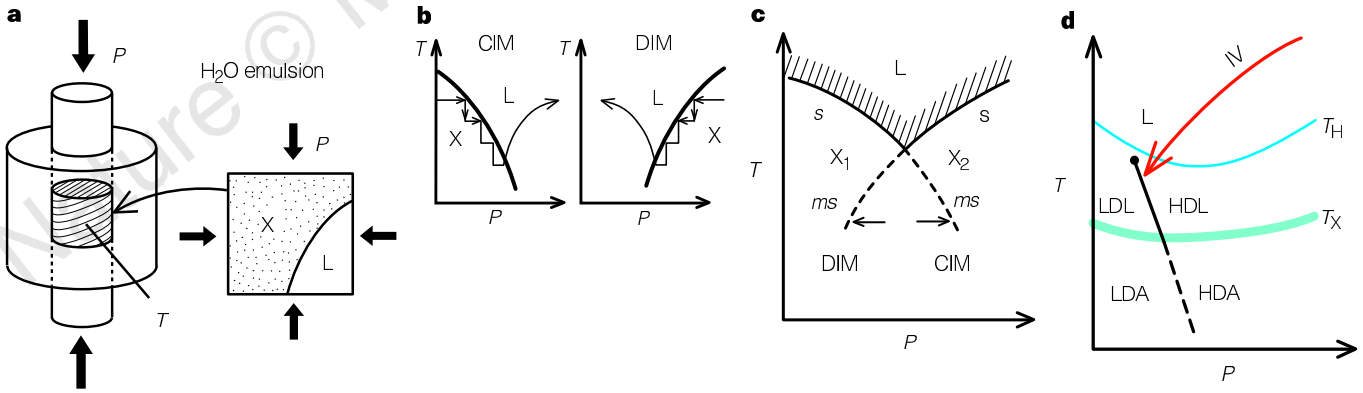

Figure 1 Overall logic of the present experiment. This experiment is designed to probe the region of the temperature–pressure phase diagram–below the nucleation temperature T_H and above the crystallization temperature T_X–where the line L_1 of liquid–liquid phase transtions might exist separating a low-density liquid phase from a high-density liquid phase. **a**, The experimental set-up. The sample, of volume ~1 cm^3, consists of 40% v/v of deionized water in a methylcyclohexane/methylcyclopentane mixture and surface stabilizer (sorbitan tristearate) and forms a water emulsion with drop diameter 1–10 μm (ref. 19). Pressure P is applied, keeping the cylinder at a nearly constant low temperature, using an automatic hydraulic pump with a relative error of ~2 MPa at 0.1 GPa, and 10 MPa at 1 GPa. The temperature T of the sample is monitored by an alumel-chromel thermocouple with a relative accuracy of ±0.02 K (ref. 21). The compression (and decompression) rate is held constant at $dP/dt \approx 0.2$ GPa min^{-1} even during transitions. Also shown is a diagram illustrating the case of compression-induced melting from crystal (X) to liquid (L). **b**, The endothermic temperature response of the sample during CIM (compression-induced melting) and DIM (decompression-induced melting). During both CIM and DIM, the crystal X is forced to melt by the pressure, which reduces the sample temperature because the melt absorbs the latent heat quasi-adiabatically. The cooled sample melts by further compression (or decompression). The diagram shows this endothermic temperature response to a sequence of four infinitesimal pressure increments during CIM (and a corresponding temperature response to a sequence of four infinitesimal pressure decrements during DIM). After the entire sample is transformed, the temperature returns to the cylinder temperature. **c**, Typical phase diagram showing two stable melting lines (solid curves, denoted *s*) separating two stable crystalline phases X_1 and X_2 from the stable liquid (the hatched region). Also shown are two metastable melting lines (dashed curves, denoted *ms*), one of which can be located using DIM and the other using CIM. Use of an emulsion suppresses the direct X_1/X_2 transitions. **d**, Schematic illustration of the present experiments. We measure the DIM line of ice IV, and search for a kink. We choose ice IV (ref. 29) because its metastable melting line is readily measurable by DIM; it appears to extrapolate to the region of the hypothesized line L_1 of liquid-liquid (LDL/HDL) transitions located between T_H and T_X and terminating at an apparent critical point (the black point).

behaviour shown by the DIM line of ice IV. We obtain PNP-XIII by the decompression-induced transition of the PNP-XIV emulsion annealed around 250 K. We obtain PNP-XIV (1) by heating emulsified HDA above T_X around 1.5 GPa, (2) by compressing supercooled liquid beyond the T_H line around 230 K, or (3) by cooling the liquid below T_H above ~1 GPa.

The smoothness of the PNP-XIV DIM line above T_X implies that L_1, if it exists, lies in a different region of the P–T diagram traversed by the DIM line of PNP-XIV. PNP-XIV may have a rather ordered structure because of the endothermic nature of the melting and immediate freezing transition below T_H (Fig. 2b, left panel) which indicates that the transition is apparently from a relatively ordered crystalline phase to a more disordered crystalline phase with net heat absorption.

We note that the DIM line of ice IV shows a sharp kink at 0.1 GPa and 215 K. To interpret this sharp kink, we calculate the Gibbs potential surface for liquid water, $G_L(P, T)$, and we consider if this surface is consistent with the possible existence of L_1. We shall see that the kink in the DIM line of ice IV may occur precisely at the line L_1 of the hypothesized liquid–liquid transition. As with all phase-transition data, our data are also consistent with the possibility[22] of no singularity at all, but rather a sharp but continuous change in the behaviour of the relevant quantities—as there must be experimental error bars on data points (and since the number of data points is

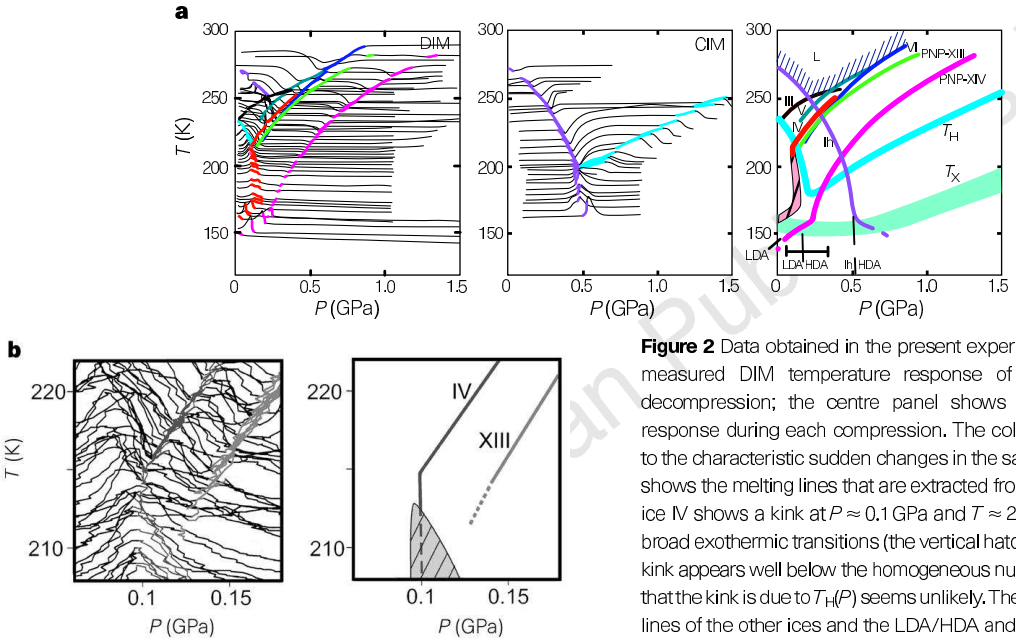

Figure 2 Data obtained in the present experiment. **a**, The left panel shows the measured DIM temperature response of the ice emulsion during each decompression; the centre panel shows the measured CIM temperature response during each compression. The colour-highlighted traces correspond to the characteristic sudden changes in the sample temperature. The right panel shows the melting lines that are extracted from the data shown. The DIM line of ice IV shows a kink at $P \approx 0.1$ GPa and $T \approx 215$ K, and is followed by the line of broad exothermic transitions (the vertical hatched region). We note also that this kink appears well below the homogeneous nucleation line $T_H(P)$, so the possibility that the kink is due to $T_H(P)$ seems unlikely. The right panel also shows the melting lines of the other ices and the LDA/HDA and I_h/HDA transition lines[20] (the long-dashed lines). The horizontal bar indicates the range of metastability found for the LDA/HDA transition. **b**, Enlargement of the region of **a** in which the kink in the DIM curve of ice IV occurs (compiling the temperature responses forms the DIM lines of ices).

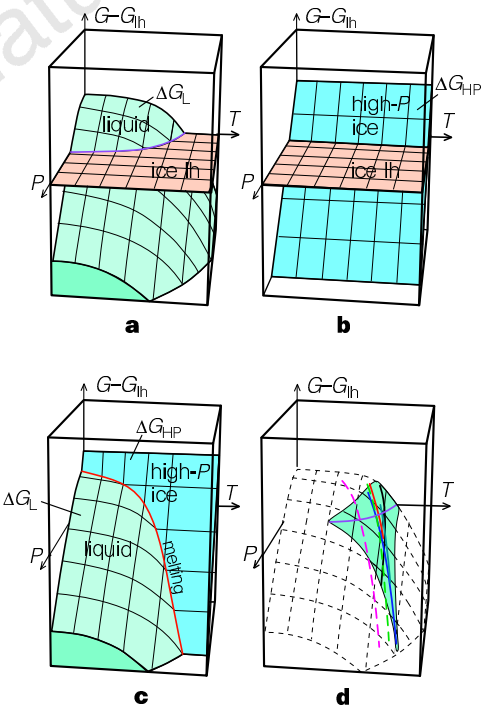

Figure 3 Gibbs potential surface for liquid water probed in the present experiments for both its stable and metastable regions. **a**, Schematic Gibbs potential of liquid water relative to that of ice I_h, $\Delta G_L \equiv G_L - G_{I_h}$. The intersection line of ΔG_L and the basal plane defines the melting line of ice I_h. **b**, Gibbs potential of a typical high-pressure ice relative to that of ice I_h, $\Delta G_{HP} \equiv G_{HP} - G_{I_h}$. **c**, The melting line for the high-pressure ice, defined by the intersection between the Gibbs potential surface of the liquid and that of the high-pressure ice. We obtain numerically the ΔG_{HP} along the melting line which must equal ΔG_L along the melting line. **d**, Schematic construction of the ΔG_L surface (the dark region) by smooth graphical interpolation between the ΔG_L potentials along the melting lines for different ices (the thick solid lines). Each of the nearly vertical thick solid lines is a melting line. The horizontal line is the melting line of ice I_h where the ΔG_L is zero (**a**). These lines locate on a surface (the ΔG_L surface: the dark region). Once we know the ΔG_L surface, we calculate the ΔG_{HP} plane for PNP-XIII and PNP-XIV, following the reverse procedure using the melting lines of PNP ice. We also estimate, and show by the thick dashed lines, the ΔG_L potentials along the melting lines of PNP ices on these ΔG_{HP} planes.

finite, not infinite) there is no *a priori* way to distinguish a function with a sharp discontinuous 'step' from a continuous function with a sharp but still continuous behaviour that merely resembles a step. An example of such a function is $y = \tanh 100x$ which appears to jump discontinuously from −1 for negative x to +1 for positive x, yet in fact is a continuous function.

The general procedure we shall follow is based on the fact that along the melting line of any solid ice phase (ice I_h, or any of the high-pressure ice phases), the Gibbs potentials of the coexisting ice and liquid phases must be identical. Hence we can obtain the Gibbs potential of the liquid phase along the melting line of each ice phase by evaluating the Gibbs potential of that ice phase along its melting line.

The Gibbs potential has no natural zero; in this study, we construct $\Delta G_L \equiv G_L - G_{I_h}$, the Gibbs potential of the liquid relative to that of ice I_h (Fig. 3a). Hence the slope of this surface with respect to P must be the difference in specific volumes of the liquid and ice I_h, and the slope with respect to T must be the difference in entropies of the liquid and ice I_h. One advantage of this construction is that the melting line of ice I_h is a curve that is constrained to lie in the plane $\Delta G_L = 0$ (Fig. 3a).

We now consider the Gibbs potential of one of the high-pressure ices relative to that of ice I_h, $\Delta G_{HP} \equiv G_{HP} - G_{I_h}$ (Fig. 3b). We can obtain the ΔG_{HP} surface by noting that to a good approximation it is a plane, because (1) the difference in specific volume between the high-pressure ice and ice I_h, $V_{HP} - V_{I_h} \equiv [\partial(G_{HP} - G_{I_h})/\partial P]_T$ is roughly constant over the relevant parameter range (0–1.5 GPa and 77–300 K), and (2) the difference in entropy between the high-pressure ice and ice I_h—that is, $S_{HP} - S_{I_h} \equiv -[\partial(G_{HP} - G_{I_h})/\partial T]_P$—is relatively small[23] (so the pressure at the phase boundary between the high-pressure ice and ice I_h is roughly constant and independent of temperature, and hence the line of intersection with the basal plane is approximately parallel to the T axis). This plane can be determined by knowing any three points or, equivalently, by knowing one point—say, the pressure at the plane's intersection with the basal plane—and the slopes of the plane in the temperature and pressure directions. We therefore calculate the ΔG_{HP} plane from its slope and the pressure at the intersection; we take the slope, $[\partial(\Delta G_{HP})/\partial P]_T = V_{HP} - V_{I_h}$, from ref. 24, and the pressure from that at the intersection between the melting line of the high-pressure ice and that of ice I_h (Fig. 2a, right panel); this is the pressure of the triple point at which three phases (liquid, ice I_h, and the high-pressure ice) coexist.

Figure 3c shows how we calculate ΔG_L along the melting line from the known ΔG_{HP} plane and the known melting line of a given high-pressure ice phase—because $G_L = G_{HP}$ along this line. We can

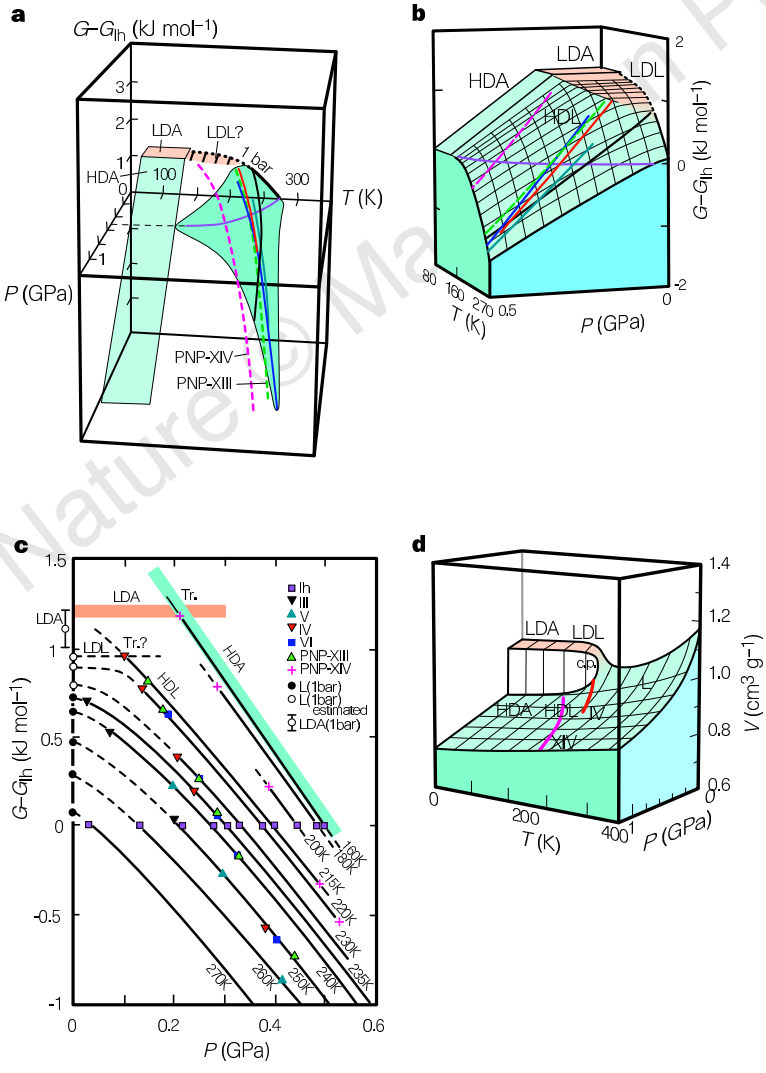

Figure 4 Application of data obtained in the present experiment to reconstruct the Gibbs potential surface and the thermodynamic equation of state $V = V(P,T)$. **a**, Comparison of the ΔG_L surface evaluated by the method of Fig. 3d (the dark region) with (1) the Gibbs potential surfaces of LDA and HDA relative to that of ice I_h, and (2) the ΔG_L at 1 bar. The LDA Gibbs potential at 150 K and 1 bar is known experimentally to be[30] 1.1 ± 0.1 kJ mol^{-1}. Also shown are ΔG_L along the melting lines of PNP ices. We find for PNP-XIII a density of 1.25 g cm^{-3}, while for PNP-XIV, we find 1.27 g cm^{-3}. The value of ΔG_L at 1 bar for $T > 235$ K (the thick solid line) we obtain from refs 25, 26, and we assume that this Gibbs potential at 1 bar is connected with the LDA potential[30] via the possible low-density liquid (LDL) state—because the liquid above 235 K, cooled extremely rapidly at 1 bar, becomes a glass which resembles LDA[31,32]. **b**, The $\Delta G_L(P,T)$ surface in the 80–270 K and 0–0.5 GPa region with constant-P and constant-T lines at 50 MPa and 10 K intervals, as evaluated from experimental data. **c**, Dependence of ΔG_L on pressure at some fixed temperatures (also evaluated from experimental data), which may be read in conjunction with **b**: the thin solid constant-T lines in **b** correspond to the lines in this figure with a reverse P-axis direction. The filled and empty circles at 0 GPa correspond to the measured and estimated potentials at corresponding temperatures at 1 bar. The LDA Gibbs potential at 1 bar is the experimental value[30]. We can draw smooth lines by interpolation between the Gibbs potential points of the ice phases, and so can construct an accurate ΔG_L surface. To connect the ΔG_L at high pressure with that at 1 bar, a rapid slope change (corresponding to a possible liquid–liquid phase transition, labelled tr.) should appear below about 220 K. **d**, Plausible qualitative equation of state $V(P,T)$ of liquid, given by the partial derivative $[\partial(\Delta G_L)/\partial P]_T$ and by adding the specific volume of ice I_h. The specific volumes of the amorphous phases are known for the region below T_X (ref. 21) and for the stable high-temperature liquid[33]. Solid lines are the specific volume along the melting lines of ice IV and XIV. The high-temperature liquid appears to separate into two low-temperature liquid phases just below the critical point located at around 0.1 GPa and 220 K; we emphasize that the data cannot locate the coordinates of the critical point, denoted c.p., with high accuracy owing to the possibility that the phase transition line might have a "hook" in it[9]. These two liquid phases are continuous with the two amorphous phases that are known to exist below ~150 K. We note that this phase transition surface differs from that of a typical liquid only in the presence of this critical point–which in turn arises because below the line of density maxima the fluctuations in specific volume and in entropy are anti-correlated by definition.

repeat this procedure for each of the high-pressure ice phases, and thereby obtain values of the Gibbs potential along an entire family of lines (Fig. 3d). Using this family of lines, we then construct the ΔG_L surface (Fig. 3d) by interpolation between the known values of ΔG_L along this family of lines.

Figure 4a shows a portion of the ΔG_L surface. As an accuracy check, we note that this surface includes on it the previously reported[25,26] line at 1 bar. Also shown are the ΔG surfaces of LDA and HDA. Thus we can calculate the entire ΔG_L surface by connecting these individual lines, and taking the slopes of the LDA phase and the hypothesized LDL phase to be similar (compare the hatched area of Fig. 4a). In this way, we find the LDA and HDA Gibbs potential surfaces, assuming that they are planes and that the I_h–HDA 'equilibrium' transition pressure is 0.5 GPa and the LDA/HDA 'equilibrium' pressure is 0.2 GPa (refs 20, 21; Fig. 2a, right panel). The slope $[\partial(G - G_{I_h})/\partial P]_T$ of LDA and HDA we obtain from their known specific volumes[15]. We note that the LDA plane is almost parallel to the basal plane because the specific volume of LDA and that of ice I_h are about the same[15]. The thick solid lines in Fig. 4a (except the line at 1 bar) are ΔG_L along the melting lines of high-pressure ices, and the thick broken lines (except the line at 1 bar) are those of the PNP ices. The error in the Gibbs potential is much less than 0.1 kJ mol^{-1}.

Figure 4b shows the results of a detailed calculation of the ΔG_L surface for T between 80 and 270 K and P between 0 and 0.5 GPa. We note that the intersection between the nearly flat LDL surface and the slope of the HDL Gibbs potential makes a distinct 'crease' which starts at the LDA/HDA boundary and continues to a point with coordinates ~0.1 GPa and ~220 K. This behaviour is consistent with the presence of a first-order transition line, as the specific volume—the first derivative of the Gibbs potential—is discontinuous across the crease.

To further test this possibility, we show in Fig. 4c the pressure dependence of ΔG_L at fixed T. For $T > 235$ K, the ΔG_L at high P extrapolates smoothly to the independently calculated ΔG_L at 1 bar. For the 220 K isotherm, the slope changes rapidly around 0.1 GPa in order to connect to the 1 bar value of ΔG_L, while at 215 K, a crease in the surface must occur if the values of ΔG_L at 1 bar and 0.1 GPa are to be on the same curve.

We note that this point (0.1 GPa, 215 K) is precisely the point where the melting curve of ice IV undergoes a sharp discontinuity, so $\Delta G_L = \Delta G_{IV}$. Although this could be a coincidence, it could also arise because of the presence of a line of first-order liquid–liquid phase transitions.

In Fig. 4d we show a possible equation of state $V = V(P, T)$ that is consistent with experimental data. The specific volumes of the two liquid phases LDL and HDL appear to be continuous with the specific volumes of LDA and HDA. Further, the anomalous behaviour of supercooled D_2O water in terms of both liquid structure[27] and molecular relaxation[28] are also consistent with the existence of a critical point with approximately the same coordinates. □

Received 6 January; accepted 9 February 1998.

1. Debenedetti, P. G. *Metastable Liquids* (Princeton Univ. Press, 1997).
2. Angell, C. A. Formation of glasses from liquids and biopolymers. *Science* **267,** 1924–1935 (1995).
3. Fourkas, J. T., Kivelson, D., Mohanty, U. & Nelson, K. A. (eds) *Supercooled Liquids: Advances and Novel Applications* (ACS Books, Washington DC, 1997).
4. Speedy, R. J. & Angell, C. A. Isothermal compressibility of supercooled water and evidence for a thermodynamic singularity at −45 C. *J. Chem. Phys.* **65,** 851–858 (1976).
5. Speedy, R. J. Stability-limit conjecture. An interpretation of the properties of water. *J. Phys. Chem.* **86,** 982–991 (1982).
6. Borick, S. S. & Debenedetti, P. G. Equilibrium, stability and density anomalies in a lattice model with core softening and directional bonding. *J. Phys. Chem.* **97,** 6292–6303 (1993).
7. Borick, S. S., Debenedetti, P. G. & Sastry, S. A lattice model of network-forming fluids with orientation-dependent bonding: equilibrium, stability, and implications from the phase behavior of supercooled water. *J. Phys. Chem.* **99,** 3781–3793 (1995).
8. Poole, P. H., Sciortino, F., Essmann, U. & Stanley, H. E. Phase behaviour of metastable water. *Nature* **360,** 324–328 (1992).
9. Tanaka, H. A self-consistent phase diagram for supercooled water. *Nature* **380,** 328–331 (1996).
10. Tanaka, H. Phase behaviors of supercooled water: reconciling a critical point of amorphous ices with spinodal instability. *J. Chem. Phys.* **105,** 5099–5111 (1996).
11. Roberts, C. J., Panagiotopoulos, A. Z. & Debenedetti, P. G. Liquid-liquid immiscibility in pure fluids: polyamorphism in simulations of a network-forming fluid. *Phys. Rev. Lett.* **77,** 4386–4389 (1996).
12. Roberts, C. J. & Debenedetti, P. G. Polyamorphism and density anomalies in network-forming fluids: zeroth- and first-order approximations. *J. Chem. Phys.* **105,** 658–672 (1996).
13. Harrington, S., Zhang, R., Poole, P. H., Sciortino, F. & Stanley, H. E. Liquid-liquid phase transition: Evidence from simulations. *Phys. Rev. Lett.* **78,** 2409–2412 (1997).
14. Sciortino, F., Poole, P. H., Essmann, U. & Stanley, H. E. Line of compressibility maxima in the phase diagram of supercooled water. *Phys. Rev. E* **55,** 727–737 (1997).
15. Mishima, O., Calvert, L. D. & Whalley, E. An apparently first-order transition between two amorphous phases of ice induced by pressure. *Nature* **314,** 76–78 (1985).
16. Mishima, O. Relationship between melting and amorphization of ice. *Nature* **384,** 546–549 (1996).
17. Bridgman, P. W. Water, in the liquid and five solid forms, under pressure. *Proc. Am. Acad. Arts Sci.* **47,** 441–558 (1911).
18. Evans, L. F. Selective nucleation of the high pressure ices. *J. Appl. Phys.* **38,** 4930–4932 (1967).
19. Kanno, H., Speedy, R. & Angell, C. A. Supercooling of water to −92 °C under pressure. *Science* **189,** 880–881 (1975).
20. Whalley, E., Klug, D. D. & Handa, Y. P. Entropy of amorphous ice. *Nature* **342,** 782–783 (1989).
21. Mishima, O. Reversible first-order transition between two water amorphs at ~0.2 GPa and ~135 K. *J. Chem. Phys.* **100,** 5910–5912 (1994).
22. Sastry, S., Debenedetti, P., Sciortino, F. & Stanley, H. E. Singularity-free interpretation of the thermodynamics of supercooled water. *Phys. Rev. E* **53,** 6144–6154 (1996).
23. Fletcher, N. H. *The Chemical Physics of Ice* (Cambridge Univ. Press, 1970).
24. Kamb, B. Structure of ice VI. *Science* **150,** 205–209 (1965).
25. Speedy, R. J. Thermodynamic properties of supercooled water at 1 atm. *J. Phys. Chem.* **91,** 3354–3358 (1987).
26. Johari, G. P., Fleissner, G., Hallbrucker, A. & Mayer, E. Thermodynamic continuity between glassy and normal water. *J. Phys. Chem.* **98,** 4719–4725 (1994).
27. Bellissent-Funel M. C. & Bosio, L. A neutron scattering study of liquid D_2O. *J. Chem. Phys.* **102,** 3727–3735 (1995).
28. Lang, E. & Ludemann, H.-D. Pressure and temperature dependence of the longitudinal deuterium relaxation times in supercooled heavy water to 300 MPa and 188 K. *Ber. Bunsenges. Phys. Chem.* **84,** 462–470 (1980).
29. Bridgman, P. W. The pressure-volume-temperature relations of the liquid, and the phase diagram of heavy water. *J. Chem. Phys.* **3,** 597–605 (1935).
30. Speedy, R. J., Debenedetti, P. G., Smith, R. S., Huang, C. & Kay, B. D. The evaporation rate, free energy, and entropy of amorphous water at 150K. *J. Chem. Phys.* **105,** 240–244 (1996).
31. Bruggeller, P. & Mayer, E. Complete vitrification in pure liquid water and diute aqueous solutions. *Nature* **288,** 569–571 (1980).
32. Bellissent-Funel, M. C., Bosio, L., Hallbrucker, A., Mayer, E. & Sridi-Dorbez, R. X-ray and neutron scattering studies of the structure of hyperquenched glassy water. *J. Chem. Phys.* **97,** 1282–1286 (1992).
33. Haar, L., Gallagher, J. S. & Kell, G. S. *NBS/NRC Steam Tables* (Hemisphere, Washington DC, 1984).

Acknowledgements. We thank C. A. Angell, K. Aoki, M.-C. Bellissent-Funel, M. Canpolat, H.-D. Lüdemann, P. H. Poole, R. Sadr-Lahijany, S. Sastry, F. Sciortino, F. W. Starr and Y. Suzuki for discussions and reading of manuscript drafts. We also thank C. A. Angell for pointing out subtle ponts that we initially glossed over. This work was supported by CREST (Core Research for Evolutional Science and Technology) of Japan Science and Technology Corporation (JST), BP and the US NSF.

Correspondence and requests for materials should be addressed to O.M. (e-mail: mishima@nirim.go.jp).

Direct measurement of tropospheric ozone distributions from space

Rosemary Munro*, Richard Siddans, William J. Reburn & Brian J. Kerridge

Rutherford Appleton Laboratory, Chilton, Didcot, Oxfordshire, OX11 0QX, UK

The role of ozone in absorbing ultraviolet solar radiation is well known. Ozone also makes a significant contribution to the radiative balance of the upper troposphere and lower stratosphere, such that changes in the distribution of ozone in these atmospheric regions will affect the radiative forcing of climate[1,2]. Furthermore, tropospheric ozone is the source of the hydroxyl radical which controls the abundance and distribution of many atmospheric constituents, including greenhouse gases such as methane and hydrochlorofluorocarbons. Tropospheric ozone is produced photochemically *in situ* and is also transported down from the stratosphere, but the relative importance of these two sources to its global budget is poorly understood. High-quality tropospheric and lower-stratospheric ozone profile measurements are available from sondes and lidar techniques, but their geographical sampling is very limited. Complementary satellite measurements of the global ozone distribution in this height region are therefore required to quantify ozone's tropospheric budget and its participation in climate-forcing and tropospheric

* Present address: ECMWF, Shinfield Park, Reading, Berkshire, RG2 9AX, UK.